Computational Modeling and Simulation of Stenosis of Aqueduct of Sylvius Due to Brain Tumor

Uzair Ul Haq
National university of Sciences & Technology (NUST)
Ali Ahmed
National university of Sciences & Technology (NUST)
Zartasha Mustansar (zmustansar@rcms.nust.edu.pk)
National university of Sciences & Technology (NUST)
Arslan Shaukat
National university of Sciences & Technology (NUST)
Sasa Cukovic
ETH Zurich
Faizan Nadeem
Institute Of Nuclear Medicine & Oncology Lahore
Saadia Talay
National university of Sciences & Technology (NUST)
Junaid Iqbal Khan
Bahauddin Zakariya University
Lee Margetts
University of Manchester

Research Article

Keywords: Cerebral aqueduct, intracranial pressures, obstructive hydrocephalus, fluid-structure interaction

Posted Date: December 1st, 2021

DOI: https://doi.org/10.21203/rs.3.rs-1116722/v1

Computational Modeling and Simulation of Stenosis of Aqueduct of Sylvius Due to Brain Tumor

Uzair Ul Haq[1], Ali Ahmed[2], Zartasha Mustansar[2*], Arslan Shaukat[3], Sasa Cukovic[4], Faizan Nadeem[5], Saadia Talay[2], Junaid Iqbal Khan[6], Lee Margetts[7]

[1]Department of Biomedical Engineering & Sciences, School of Mechanical & Manufacturing Engineering (SMME), National university of Sciences & Technology (NUST), Islamabad 44000, Pakistan.

[2]Department of Computational Engineering, Research Center of Modelling & Simulation, National university of Sciences & Technology (NUST), Islamabad 44000, Pakistan.

[3]Department of Computer & Software Engineering, College of Electrical & Mechanical Engineering, National university of Sciences & Technology (NUST), Islamabad 44000, Pakistan.

[4]Institut für Biomechanik, HCP H 17.2, Leopold-Ruzicka-Weg 4, 8093 Zürich, Switzerland

[5]Institute of Nuclear Medicine & Oncology Lahore (INMOL), Lahore, Pakistan

[6]Laboratory of Theoretical and Experimental Physics, Bahauddin Zakariya University, Multan, Pakistan

[7]Mechanical and Aeronautical Engineering Division L5, Department of Mechanical, Aerospace & Civil Engineering, The University of Manchester

*Correspondence: zmustansar@rcms.nust.edu.pk

Abstract

Background: Stenosis of cerebral aqueduct (CA) is featured in many studies related to elevated intracranial cerebral pressures (ICP). It also presents a challenging situation to clinicians. Compressive forces play a lead role in pathological situations like tumor presence and hence can cause obstruction to the flow of cerebrospinal fluid (CSF). Due to this barrier, excessive retention of CSF in ventricles can occur. This in turn could contribute to increased pressure gradients inside the cranium. In literature, most of the numerical models are restricted to modeling the CSF flow by considering ventricle walls as rigid material unlike its behavior a deformable character. This paper, therefore, addresses the same from a holistic perspective by taking into consideration the dynamics of the flexible character of the ventricular wall. This adds to the novelty of this work by reconstructing an anatomically realistic ventricular wall behavior. To do this, the authors aim to develop a computational model of stenosis of CA due to brain tumor by invoking a fluid-structure interaction (FSI) method. The proposed 3D FSI model is simulated under two cases. First, simulation of pre-stenosis case with no interaction of tumor forces and secondly, a stenosis condition together-with dynamic interaction of tumor forces.

Results: Comparing the forces with and without tumor reveals a marked obstruction of CSF outflow post third ventricle and the cerebral aqueduct. Not only this but a drastic rise of CSF velocity from 21.2 mm/s in pre-stenosis case to 54.1 mm/s stenosis case is also observed along with a net deformation increase of 0.144 mm on walls of ventricle.

Conclusions: This is a significant contribution to brain simulation studies for pressure calculations, wherein the presence of tumors is a major concern.

Key terms— Cerebral aqueduct, intracranial pressures, obstructive hydrocephalus, fluid-structure interaction.

1. BACKGROUND

Brain tumors can be of benign or malignant. Compressive forces of brain tumor may constrict the flow of Cerebrospinal fluid (CSF), thereby causing stenosis of cerebral aqueduct (CA). Likewise, during stenosis of CA, obstructive hydrocephalus (which is one of the direct consequences of constriction caused by brain tumor on walls of CA) could be seen as well. Understanding the underlying mechanisms of stenosis of CA, nature, pathophysiology and biomechanics of brain tumor and obstructive hydrocephalus viz a viz their relationship with each other can be understood well. The study of stenosis of CA can also aid in better understanding the rise of intracranial pressures (ICP) under special circumstances. According to a survey conducted by [1] around 23,890 adults in the United States of America are diagnosed with brain cancers this year; and whereas, every year about a million Americans are affected by Hydrocephalus [2]. Stenosis of cerebral aqueduct (CA) is an important domain and catchy topic clinically to discuss. Since continuous monitoring of CSF pressure (and ICP) inside the cranium usually involves surgical interventions. The invasive mechanisms for clinically sensitive procedures are risky and cannot be used, as a matter of routine. However, a numerical-based model may address this clinical and practical limitation in a non-invasive manner. This can provide clinicians better analytics methods to understand brain tumor interaction with walls of CA and its effects, including stenosis without surgical interventions.

CSF modeling exhibits fluid flow in brain noninvasively. For this purpose, computational fluid dynamics (CFD) has been widely used to model fluid flows for biomedical applications. Many studies provide evidence for the same including Jacobson et al. [3] which consists of a simple cylinder to study the flow of CSF through of CA. This study suggests that pressure difference of at least 1.1 Pa is required to drive the CSF from CA. In another study [4], a synchronized framework is proposed by considering two models, a cylindrical rigid wall model and an elastic wall model segmented from MRI data to study flow of CSF in CA. The spatial domain was digitized using Immersed Boundary method (IBM) [5]. Pulsatile velocity inlet boundary condition is used, and their results show pressure drop of 1.02 Pa and velocity of 30.20 mm/s for cylindrical model. Whereas for elastic wall model, the pressure drop of 2.91 Pa and

velocity of 64.65 mm/s was observed. This drastic change in pressure while considering deformable model of ventricles is important. It raises questions on assumptions of rigid wall model of ventricles. A. A. Linninger et al. [6] proposed a 2D rigid model of human ventricular system (HVS) where a pressure drop of less than 2 Pa and velocity of 7.3 mm/s is reported. In one of the extensive studies on CSF flow employing HVS, Howden et al. [7] 3D Ventricles were segmented from MRI data and CSF was treated as incompressible Newtonian fluid [11]. Pulsatile velocity inlet and zero-gauge pressure at outlet boundary conditions were used. The maximum velocity and Reynolds number was found to be 11.38 mm/s and 15 in CA respectively. Similarly, in a study by Vartan Kurtcuoglu et al. [8]., authors provided a guided framework using simplified geometry of ventricles and compared their case with the simplified geometry of stenosed. This study concluded a rift in pressure amplitudes and peak velocities change relative to the case of stenosis. The study further concludes that under a stenosed CA, *pressure amplitude in the lateral ventricles increase as stenosis level increase*. Study of Jacobson et al. [9] also suggests that under mild stenosis, pressure required to initiate CSF flow increases to 125 Pa. A conclusion of this work reveals an increase in the "*Transmantle pressure*" pivotally, even with little changes in intraventricular pressures.

One such approach is Fluid structure interaction (FSI). Three papers are the most relevant in this context. First, Masoumi et al [10]; this paper presented a 2D FSI model of ventricular system and a simulation of CSF flow inside ventricle. A deformation of 0.006 mm on the walls of ventricles is reported. However, they used a 2D model. Second study was proposed by Gholampour S. [11]; which modeled a *non-communicating hydrocephalus case* and provided a 3D fluid-structure interaction (FSI) model of CSF in simplified Subarachnoid space and ventricles geometry. The aim was to look into model behavior in hydrodynamics of CSF under differing situations. This study is relevant in terms of developing a 3D FSI model. Third one was the study by Sweetman and A. Linninger [12] in which a 3D FSI model is developed for studying the CSF flow inside the Central Nervous System (CNS). Using these two studies, a similar 3D FSI model is developed for studying stenosis of CA.

Literature gives a valuable insight to study the stenosis of cerebral aqueduct. However, most of the studies oversimplifies the model. First, assuming the *rigid wall behavior* of ventricles and resorting to mere simple flow analysis, instead of considering the *deformable nature of ventricles*. Secondly, while considering ventricular walls as rigid, one cannot model the effect of the external forces, such as forces originating from brain tumor, onto the behavior of intraventricular CSF flow. Hence, to study stenosis of CA the aforenoted infirmities need to be addressed. Briefly, a different approach for modeling stenosis of CA is needed which forms the base of our work.

The science of the present study relies on building a 3D FSI model which combines both the structural and fluid dynamics into a single framework. We have made an effort to show a complete understanding of the stenosis CA, that too by considering realistic conditions i.e. deformable ventricular wall property and its relative fluid response. In the later section, we have also incorporated the effect of pulsatility, as discussed above. Overall, the proposed model has maximum fundamental features associated to it and can be applied in various cases apart from this specific example.

The remainder of the paper is organized into following sections: *(i)* description of material and methods under which various procedural, numerical and simulation settings are discussed; *(ii)* Results of the simulation; *(iii)* Discussion on the results obtained and limitations of the present study.

2. RESULTS

ANSYS software was used for the simulation of model. It provides system coupling toolbox through which structural and fluid solvers can be united together via strong coupling method (having same timestep sizes) so that data transfer occurs at the same timestep between the solvers. Timestep size used in this study is taken to be 0.01 seconds. Results are mentioned below against various important parameters:

3.1 Model Validation

Segmented tumor and ventricles from the MRI datapoint were validated as well. A comparison of volumes of both segmented and ground truths (provided by the Radiologist) is provided in Table 2. The percentage error with reference to the ground truths for ventricle and tumor stands at 4.18% and 3.93% which is acceptable since large deviations have been eliminated. Hence in terms of geometry, model is largely validated within generally acceptable limits of 5% error.

Table 2
Ventricular and Tumor Segmentation Validation

Specimen	Ventricular Volume			Tumor Volume		
	Segmented Volume (ml)	Ground truth Volume (ml)	Percentage error	Segmented Volume (mm^3)	Ground truth Volume (mm^3)	Percentage error (%)
MRI Image	25.32	24.32	4.18%	997.29	959.51	3.93%

3.2 CSF Flow Field and Reynold's Number under Stenosis of CA

Velocity field is one of the important parameters in CSF modeling, CSF peak velocity always occurs in the cross-section of CA due to narrow pathway. The simulation results are presented for two cases.

First case pertains to FSI simulation of ventricular body with no interaction of tumor forces. Fig 7. shows vector plots of velocity in third and fourth ventricle at different timesteps for cases wherein tumor forces act on walls of CA to ensue different levels of stenosis. Fig 7 (a) pertains the case when the tumor forces are minimum and 10% stenosis in the CA is observed. Fig 7 (b) and (c) shows the steady rise in the CSF velocity due to the narrowing of pathway because of increasing tumor forces. However, after some time tumor forces increases to a greater magnitude constricting further the pathway of CA. This constriction corresponds to the maximum stenosis of CA due to which velocity rises drastically to 54.1 mm/s depicting that the duct has deformed considerably, relative to the previous stenosis levels. Fig 7 (d), shows that the velocity vectors at the point constriction have started to change direction as well. This suggests that the deformable property of ventricle should not be overlooked because it has visible effect on the biomechanics of the system.

In addition to this, another useful parameter to gauge the dynamics of CSF under the scenario of stenosis of CA was to find out Reynold's number of the flow. Reynold's number is another important parameter which signifies the transition of flow from laminar to turbulent. It is given by:

$$Re = \frac{\rho \vartheta D}{\mu} \tag{13}$$

From equation (13), Reynold's number is directly proportional relation to the velocity which also suggest that as flow velocity increase, so does the Reynold's number. Flow in lateral ventricles is in order of 10^{-3} mm/s which clearly shows characteristics of creeping flow. Consequently, in terms of Reynold's number in lateral ventricles there is no noticeable effect. However, flow velocity in CA changes abruptly and so does the Reynold's number. While for case presented in Fig 7 (a), Reynold's number is found out to be 38.5, however, for the case presented in Fig. 7 (d) where 75% stenosis is observed it rises to 110. The maximum Reynold's number is found to be 110 which suggests that the CSF flow in CA is overall laminar. However, a stenosed CA represent a complex situation wherein flow profile, velocity and Reynold's number change significantly and may pose clinical complications.

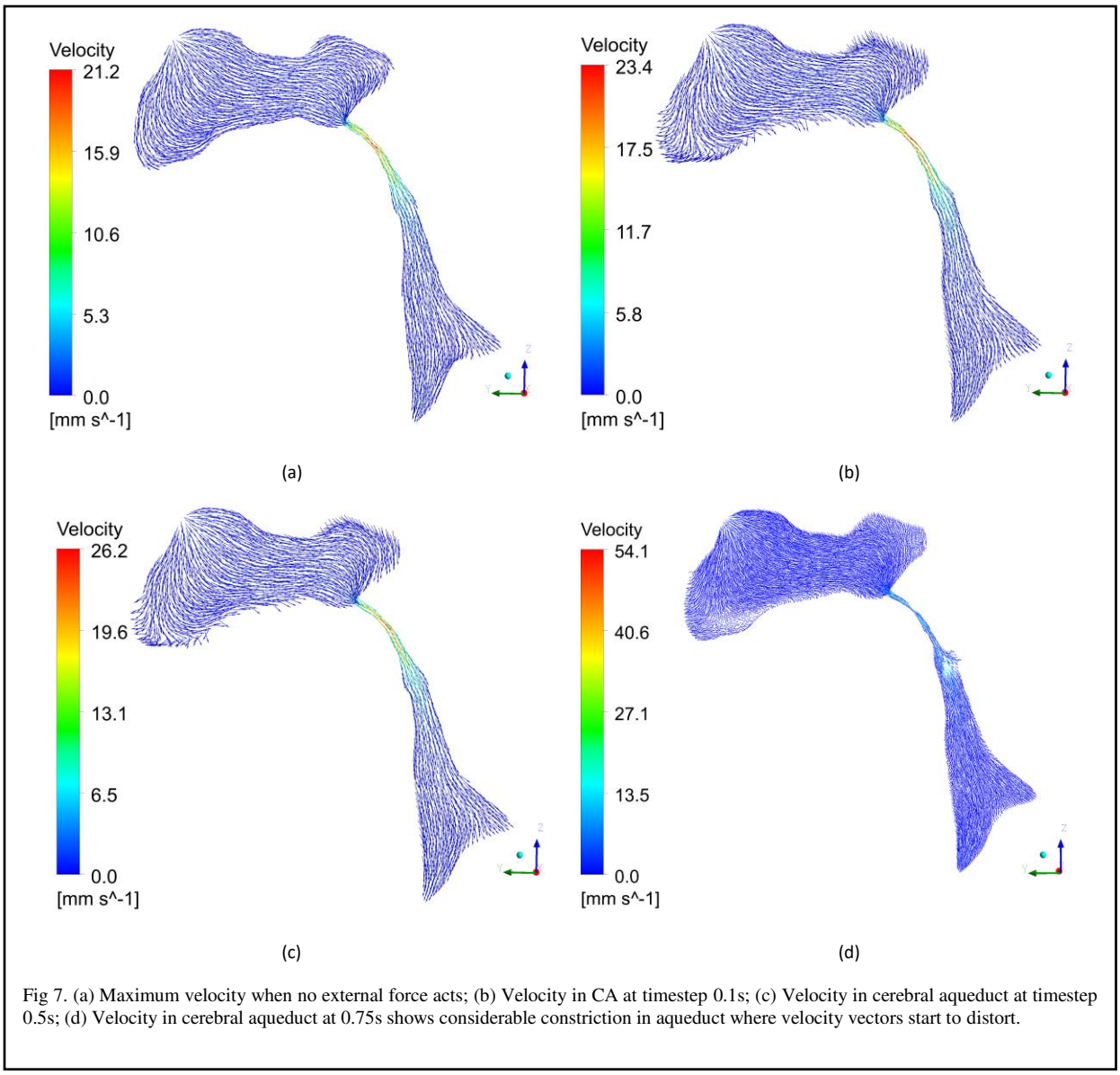

Fig 7. (a) Maximum velocity when no external force acts; (b) Velocity in CA at timestep 0.1s; (c) Velocity in cerebral aqueduct at timestep 0.5s; (d) Velocity in cerebral aqueduct at 0.75s shows considerable constriction in aqueduct where velocity vectors start to distort.

3.3. Ventricular Wall Pressures

Ventricles are cavities containing CSF fluid. CSF pressure on the walls of ventricles is important fluid dynamic variable which drives flow through any media via pressure difference. From Fig 1, it can be seen that ventricles are four, which are interconnected cavities through different channels such as foramen of Monro and CA. Among them, lateral ventricles are larger in volume and space, and the rest are relatively smaller than lateral ventricles. Hence pressure gradient and amplitude ought to be larger in lateral

ventricles. A larger pressure variation also determines the Transmantle pressure. A transmantle pressure is the net pressure gradient across the parenchyma all the way till the subarachnoid space. Resultantly, if transmantle pressures are high due to high intraventricular pressure then patient may confront with the case of elevated ICP. Simulation results determine whether transmantle pressures increase under the case of stenosis of CA, comparable to that of non-stenosed duct which would also depict a corresponding difference in cases for elevated ICP, if any.

Figure 8 shows results of pressure field distribution on walls of ventricles. Fig 8 (a) pertains to the case of a healthy brain where no tumor is present. In this case, a maximum pressure of 2.5 Pa is observed. It is also observed that the pressure variations in large cavities such as lateral ventricles were found to be spatially uniform. This is perhaps because of their large size. Pressure drop of 0.2 Pa and 1.7 Pa is found across the third ventricle and CA. A large pressure drop across CA is observed to due narrow pathway resulting in greater pressure drop.

Fig 8 (b) pertains to the case of a tumor specific cased where pressure field is reported for a stenosed CA. In this case, a higher pressure in lateral ventricles is observed due to decreased outflow towards fourth ventricle. Maximum pressure of 5.4 Pa is found in the lateral ventricles, with a pressure drop of 0.8 Pa in the third ventricle. Pressures in CA present a unique case. A stenosed duct is practically a duct which is squeezed to a point where ideally there is no outflow. Hence, beyond that point no fluid enters which makes pressure in that section to drop below the surrounding pressures. This confirms that under stenosed CA, pressure in the CA and fourth ventricle drop significantly and pressures in lateral ventricles increases, indicating distention of lateral ventricles.

Fig 8 (c) shows wall shears on the walls of CA and fourth ventricle. Wall shear stress is an additional feature which contribute towards valuable analysis in this study. In a stenosed CA, force acts on walls of CA, this causes fluid layers to abruptly overlap with each other, in the localized region, causing velocity to change significantly resulting in high shear stresses. A non-stenosed CA does not give high wall shear stresses (has stresses of order 10^{-2} Pa) which suggest that normally CSF flow has laminar profile.

However, under the influence of tumor, shear stress rises to 25 Pa. This additional parameter is a significant contribution to understand flow mechanics in the presence of tumor.

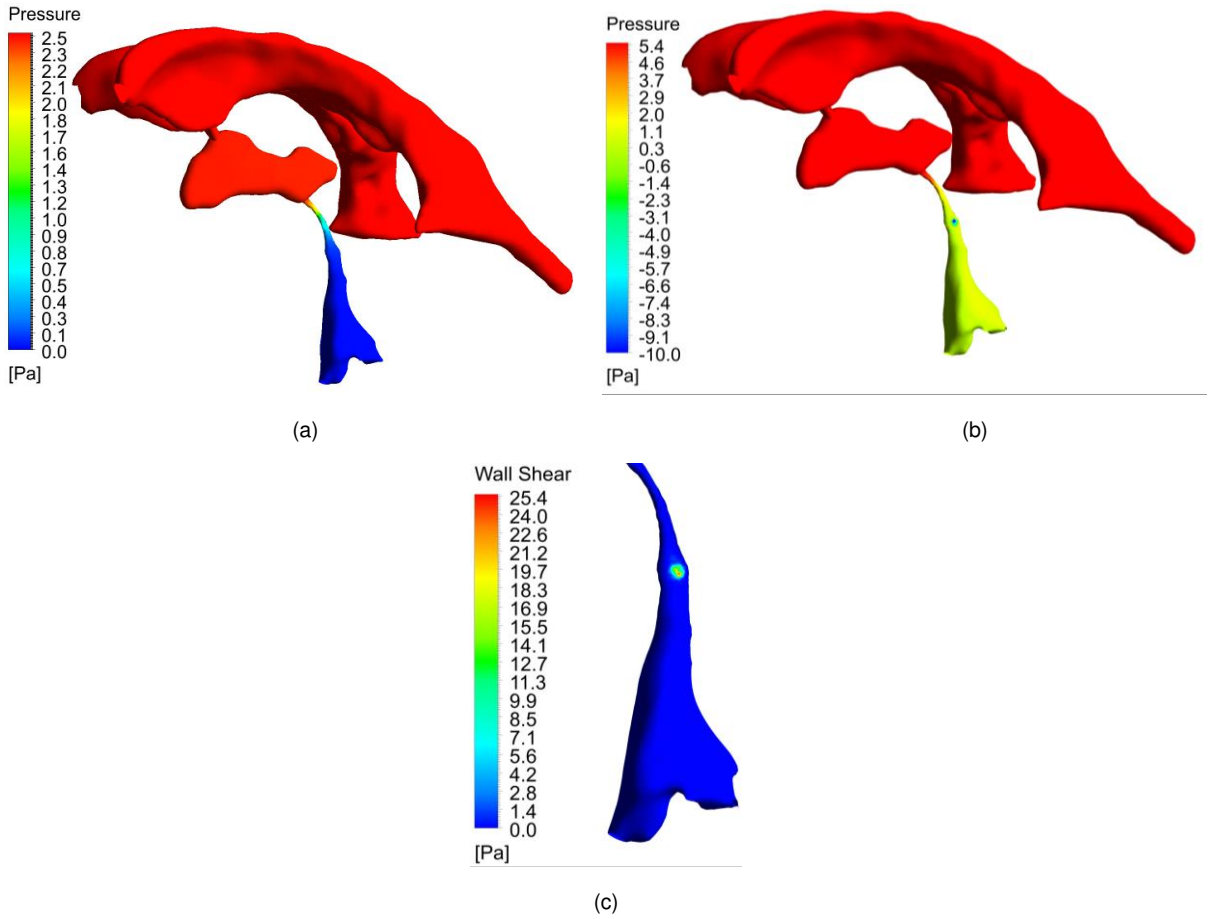

Fig 8. Pressures on the walls of ventricles. (a) shows pressure distribution on the walls of ventricles when no tumor force acts; (b) shows pressures on the walls of ventricles when tumor force acts; and (c) is the wall shear created due to tumor force.

3.4 Deformation on Walls of Ventricles.

Since walls of ventricles have been modeled as elastic therefore their deformable character results in deformation. Figure 9 show the deformation field obtained on the walls of ventricles under two cases. *Case 1*: Fig 9 (a) pertains to the case of non-stenosed CA. It shows a usual and nominal deformation of 2.0um.

Case 2: Fig 9 (b) shows a tumor specific case. In this particular case, a drastic increment in deformation of 0.146 mm in lateral ventricles is observed.

This deformation shows that once the CSF flow is obstructed considerably, pressure in lateral ventricles increase and deform the lateral ventricles. It also creates a requisite compliance for the excessive retention of CSF fluid which cannot flow towards fourth ventricles due to constriction. Since this particular case has not be modeled even in 2D hence the values presented herein can only be interpreted intuitively.

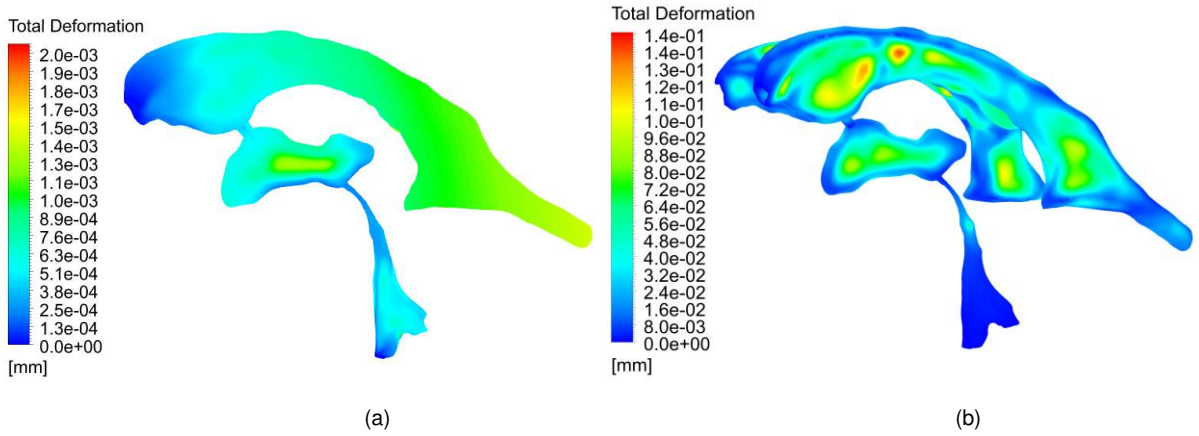

Fig 9. Deformation distribution on walls of ventricle. (a) shows deformation when no tumor is acting, (b) shows increased deformation due to the action of tumor force.

3.5 Effect of Considering CSF Pulsatility on Stenosis of CA

The pulsatile component of CSF is induced due to the blood flow in cerebral vasculature during a cardiac cycle. Pulsatile mass flow inlet is provided using equation (10). Figure 10 shows the simulation results because of cardiac cycle on the flow of CSF in ventricles.

Fig 10 suggest that the pulsatile component of CSF has drastic influence on the CSF velocity which rises to 58.21 mm/s. The motion of cerebral vasculature pushing and driving CSF flow creates additional force which produces motion of CSF in ventricles Deformation observed on the walls of ventricles does increase when considering the pulsatile nature of CSF. As stated above, the deformation observed on the

walls of ventricles under the stenosed CA is 0.146 mm; while accommodating pulsatile nature, the deformation increases to 0.40 mm.

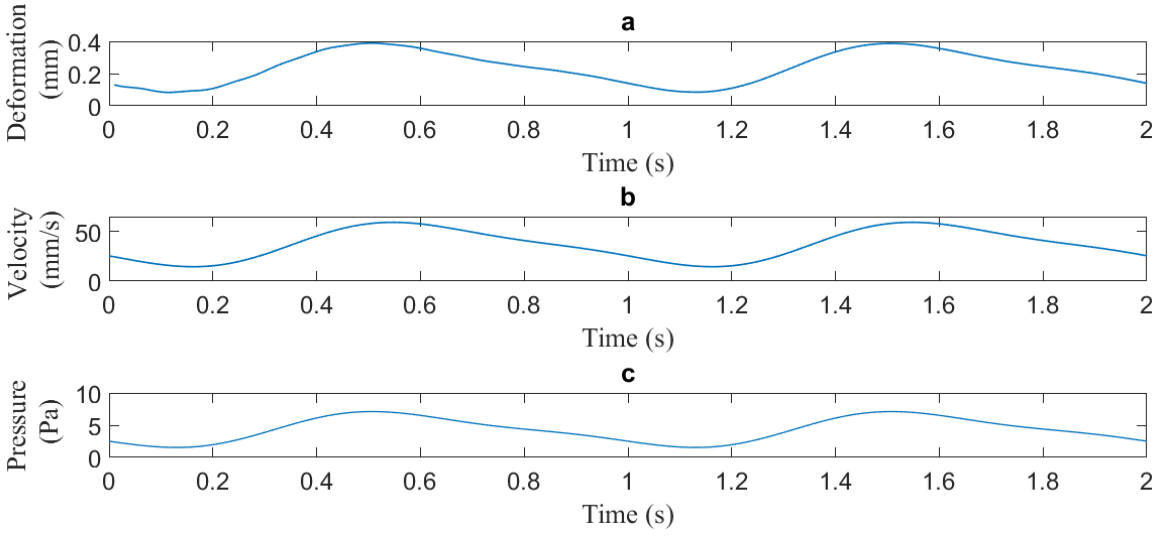

Fig 10. Graphs of Deformation on walls of ventricles (a); velocity in the Cerebral aqueduct (b); and Maximum pressure variation in lateral ventricles.

4. DISCUSSION

The proposed study presents a 3D FSI model of stenosis of CA due to the compressive forces of brain tumor. Our work is an effort to provide a basic framework from which any ventricle-CSF interaction can be studied. For better visualization, two cases are simulated, with and without interaction of tumor. This comparison allows us to visualize differences between the two conditions. For these two cases, various flow parameters such as CSF velocity, pressures (aka Transmantle pressures), Reynold's number and deformation values are calculated. The role of CSF pulsatility is also catered in the proposed model for realistic model interpretation. The results of this study show that impact of the deformable character of ventricle wall is significant. CSF velocity and Transmantle pressures increase significantly at the obstruction phase, initially from 21.2mm/s in pre-stenosis case to 54.1mm/s stenosed case and

accompanied with a net deformation increase of 0.144mm on walls of ventricle. These results are benchmarked against the results present in the literature.

It is important to discuss here how the results were validated. Validation of results were carried out via two independent sources. First, we validated our results with the past models of FSI presenting case studies of CSF flow parameters. Second source of validation was PC-MRI studies, taken from the literature, which provide experimental results for CSF flow parameters. Table 3 provides the results of present case and compares it with previous FSI-based papers and Table 4 provides PC-MRI studies reported in literature. As evident from table 3, our proposed study is compared against previous papers of either simple CFD modeling or by FSI papers such as Jacobson et al. [3], Fin and Grebe [4], Linninger et al. [6] Kurtcuoglu et al. [8], Howden et al. [7], Masoumi et al. [10]. Results against our proposed model are better inasmuch as that our model presents a 3D FSI model and also presents better explanation and improved characterization of flexible character of ventricles than Masoumi et al. [10] study. Whereas, studies by Jacobson et al. [3], Fin and Grebe [4], Linninger et al. [6] Kurtcuoglu et al. [8] and Howden et al. [7] are limited to-date as they consider ventricular surface as rigid. Table 4 presents some basic Cine-Phase contrast MRI studies for CSF volume and velocities. This is just an additional parameter to correlate and validate velocities. These studies include Abbey et al. [20], Algin et al. [21] and Lee et al. [22]. Obviously, accurate depiction of velocity for a particular case may not be available but these results do present an indirect correlation or validation. Furthermore, at various stenosis level (10-75%) graphs are plotted of velocity, pressure and Reynold's number which are provided in fig 10. This is done to better visualize the changing character of these parameters at different percentages of stenosis level.

From a theoretical and practical perspective, we conclude that various flow parameters, magnitude and location of tumor forces affect the outcome. One important parameter is Transmantle pressure. Higher the Transmantle pressure higher would be the distention/deformation on the ventricular body. The same has also been alluded in the study by Holmlund et al. [23-24]. Whereas, CSF pulsatility amplifies and

1 increases Transmantle pressures. Hence another point of conclusion is the physiological role and
2 importance of pulsatility in 3D FSI calculation of CSF in intraventricular and intracranial regime.

Table 3
Comparison of results from the Proposed Method to Previous FSI based Papers (With 25% stenosis, velocity increased by 30%)

Study	Velocity (mm/s) in CA	Pressure drop (Pa)	Deformation (mm)
Jacobson et al. (1996) [3]	28	<1.1 for CA	Walls modeled as rigid
Fin and Grebe (2003) [4]	64.65	2.91 for elastic wall model for CA	Implemented flexible cylindrical wall model of CA and obtained 0.61 mm deformation
Linninger et al. (2005) [6]	25.8/-21.7	2 in CA	No deformation reported. However, net increase of ventricular volume of 4.5% is reported.
Kurtcuoglu et al (2005) [8]	With 25% stenosis, velocity increased by 30%	With 25% stenosis, intraventricular pressure increased 8.9%	No deformation reported.
Howden et al. (2008) [7]	11.38	1.14	Walls modeled as rigid
Masoumi et al. (2013) [10]	8/-6	< 2	Normal CSF-Ventricular interaction: 0.006 mm
Proposed Method	Without tumor interaction: 21.2 Stenosis of CA: 54.1	Without tumor interaction: 2.5 Stenosis of CA: 5.4	Without tumor interaction: 0.002 mm Stenosis of CA: 0.146 mm

3

Table 4
Comparison of Results of Proposed Method to PC-MRI Studies reported in Literature

PC-MRI Study	Stroke volume (mL/beat) (±SD)	Peak velocity Craniocaudal cm/s (±SD)
Abbey et al (2009) [20]	0.017±0.010	3.24±1.08
Algin et al (2010) [21]	0.039±0.039	4.78±2.48
Lee et al (2004) [22]	0.02±0.0125	3.39±1.61
Proposed Method	0.006±0.01	Without tumor: 2.1 With tumor: 5.4

4

5. LIMITATIONS

There are limitations associated with this study too, which needs to be discussed here. First limitation is the factor of gravity. Gravity affects the flow of fluids generally. However, if the flow is single-phase and fluid is incompressible (which CSF is in proposed case) then gravity produces little effect on the flow field because when there is no net change in density, the fluid forces will be exactly the same and counter-acting against the gravity forces.

Second is the factor of slight pulsations caused by respiration (similar to cardiac induced pulsations). In cases where breathing is normal, CSF movement is little influenced by normal thoracic breathing [25], however, if deep excursions and abdominal breathing is considered then it can be presumed that it may induce some effect on the CSF flow [26].

Third factor which was in the larger perspective but was not taken into account in this study is that we have mainly focused on the tumor forces due to the solid core contributing body forces and have neglected the fluid component. Though tumor ‘s solid core is essentially made up of extracellular matrix and collagen fibers which by far has the largest contribution towards tumor forces and can be assumed to approximate around this force, however, taking fluid forces also may introduce further improvement in the model. It also helps in understanding behavior when the growing extracellular matrix has either ruptured (due to hydrostatic forces) or it has created a cerebral edema in its vicinity. Hence if edema is present, it would be better advised to consider the effect of fluid hydrostatic pressure.

Fourth, we have applied tumor forces on the walls of ventricles. This simplification allows us to understand the biomechanical behavior and physiology of stenosis of CA. This approach is best suited when considering intraventricular tumors. However, if the tumor is on any other location, then either the interaction of brain parenchyma needs to be taken or a transformation matrix is needed to find the transmission factor with which forces are either reduced or increased (as the case may be) as they travel

through the brain parenchyma. Further, usually a force field or body forces may be enough to find the major effect of tumor on walls of CA. However, sometimes stress field is also needed if brain parenchyma interaction is considered.

Lastly, CSF biomechanical model is constructed by segmenting anatomically realistic brain ventricles. We did not consider effect of Subarachnoid space (SAS) where 75% of CSF volume is usually found. The purpose of not considering (SAS) in this study pertains to the fact that the biomechanical properties, flow parametrization and Transmantle pressure distributions are largely driven or influenced by changes in biomechanical behavior of CSF in ventricular regions apart from CA. For instance, obstructive hydrocephalus is caused due to stenosis of CA thereby increasing ICP; changes of CSF velocity in subarachnoid space are negligible because it is a large cavity, and thus creeping flow dominates. Therefore, while analyzing CSF biomechanical properties, another dimension of studying the behavior of CSF inside the ventricles may be a useful parameter.

6. CONCLUSION AND FUTURE WORK

This paper is to the best of our knowledge the first effort which model stenosis of CA under the influence of brain tumor using FSI modelling. Our work shows that by using image informatics coupled with FSI modeling, the underlying ventricular-CSF interaction can be well established and understood. Furthermore, model proposed is not only restricted to the particular case at hand but can also be extended to other cases where CSF-ventricular interaction is under consideration. For future work, we hope to extend our proposed work and include particularly three aspects in our model. The factor of subarachnoid space and brain parenchyma interaction which will define a complete intracranial environment during the CSF-ventricular interaction. Second factor which can be included in future is the role of fluid forces of tumor which may influence the outcome especially if they are accompanied by cerebral edema. Lastly, we hope to incorporate in our model, role of blood-brain barrier and cerebral vasculature so as to obtain more accurate and closer representation of pulsatile nature of CSF.

3. MATERIALS AND METHODS

2.1 Subject Specific MRI Image and Clinical Characteristics

MRI image used in the instant study is a T1-contrast enhanced image acquired from 1.5 Tesla machine. The spatial dimension of MRI image acquired is 512x512x288 mm^3. Slice thickness in z-dimension is approximately 0.6mm. Ventricular and tumor geometries are segmented using 3D Slicer. The geometry is further refined by using Laplacian smoothing filter. Figure 1 shows axial scan of MRI data and segmented ventricle and tumor body.

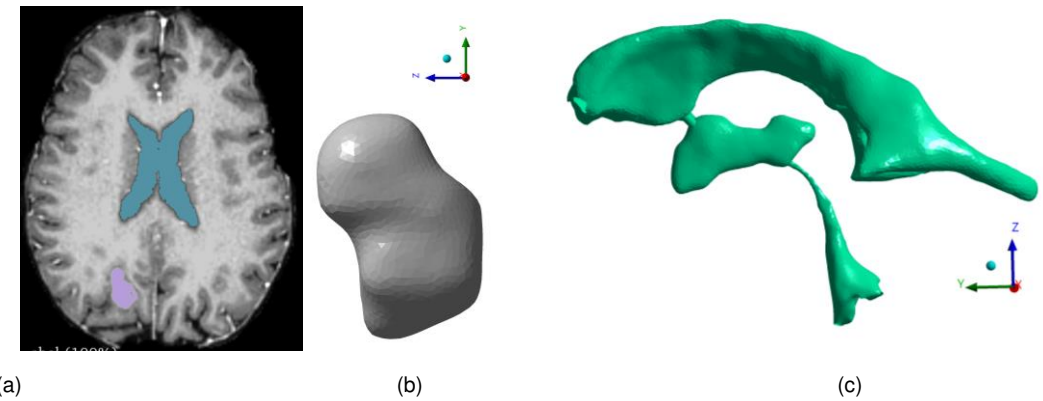

Fig 1. MRI data. (a) shows axial scan with tumor and ventricle region highlighted; (b) and (c) shows 3D tumor and ventricle geometry reconstructed.

2.2 Meshing of Geometry and Mesh Independence Test

Mesh independence study is performed to find the ideal grid size. As Fluid-Structure Interface technique is used therefore performing mesh independence test on fluid and structure domain separately gives better indication of the converged solution. In solid domain, SHELL 181 elements were used. This ensured a less computational load. A static structural solution was applied under a specified pressure and maximum stress value was recorded. After mesh independence test, a grid size of 196576 elements with minimum element size of 0.3 mm was preferred which was fine enough to capture all the physics in the

simulation. Similarly, in the case of fluid domain, tetrahedral elements (SOLID 187) were used for meshing. Mesh independence study was carried out to identify an ideal grid size. Results, confirmed that a mesh density of 1144379 elements with minimum element size of 0.5 mm was good enough to capture all the important information regarding peak velocity changes in the simulation. Figure 2 shows the meshing of geometry and Fig 3. shows the mesh independence study for both solid and fluid domains.

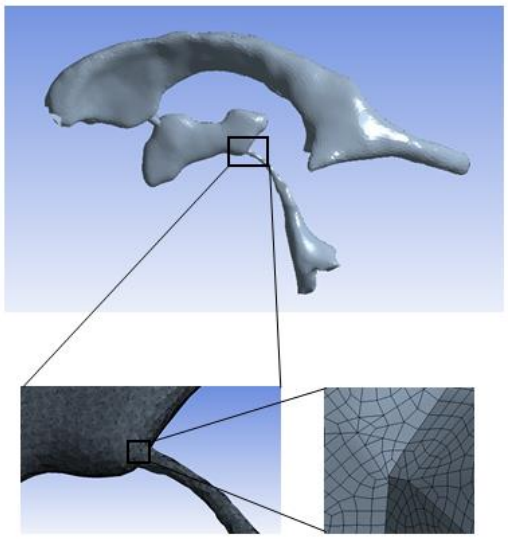

Fig 2. Meshing of 3D-model

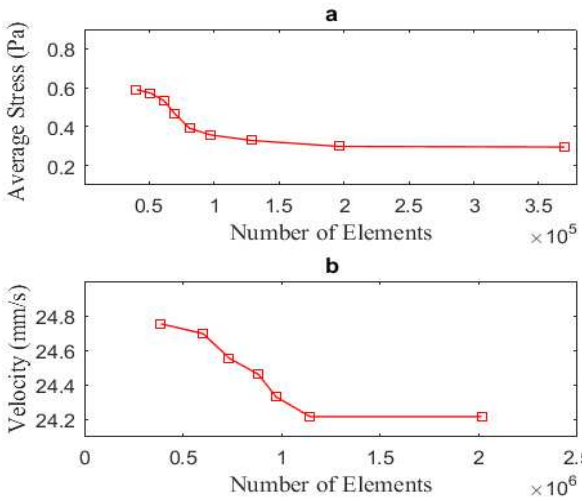

Fig 3. Grid independence study; a shows mesh independence for solid domain and b shows mesh independence for fluid domain.

2.3 Material Properties: Solid Domain

Choice of material properties for ventricular geometry was the most critical part of this study, since it is responsible for overall model behavior. Density of ventricular geometry and the poisson ratio was taken as 1000 kg/m^3 and 0.49 respectively [10]. The only thing that must be taken into knowledge here is that, in literature a ventricular geometry is largely modeled as elastic when it is studied in an isolated environment. Masoumi et al. [10] reports modulus of elasticity for ventricular geometry in range of 10-30 KPa. Furthermore, it is also well established that the ventricle geometry is a soft tissue geometry and can have anisotropic or non-homogenous properties or may also have non-elastic nature when taken together with the brain tissue [13]. Such as Sweetman et al. [12] who modeled the Subarachnoid FSI boundary as Neo-Hokean. But the true biomechanical nature of ventricles is still debatable and is subject

to the availability of data from in-vivo studies. Prevailing data in the literature suggests that ventricles get the properties of its surrounding tissues such as viscoelastic [13]. Since we are considering it in an isolated environment, a linearized model was preferred in the literature [10]. Table 1 shows the material properties.

Table 1

Material Properties and Boundary Conditions

Boundary Conditions	Value	Reference
CSF Density	1000 kg/m^3	Masoumi et al [10]
CSF viscosity	0.001003 Ns/m^2	L.Howden et al [7]
Bulk mass flow	6.25x10^{-6} kg/s	Masoumi et al [10]
Pressure outlet	Zero Pascal	L. Howden et al [7]
Modulus of Elasticity	30 KPa	Masoumi et al [10]
Ventricles Tissue Density	1000 kg/m^3	Ibid
Poisson's ratio	0.49	Ibid

2.4 Governing Equations

The numerical model on the fluid side consists of solving equations of conservation of mass and momentum [14] given below:

$$\nabla.(\rho.\vec{v}) = 0 \tag{1}$$

$$\rho\frac{\partial\vec{v}}{\partial t} + \rho(\vec{v}.\nabla)\vec{v} = -\nabla P + \tau\rho + \mu\nabla^2\vec{v} \tag{2}$$

where ρ is the density of fluid, v is the velocity of the fluid, ∇ is the gradient operator, $\rho\frac{\partial\vec{v}}{\partial t}$ is the local acceleration of fluid particles, $\rho(\vec{v}.\nabla)\vec{v}$ is the convective acceleration, ∇P is the pressure gradient, $\tau\rho$ are body forces, $\mu\nabla^2\vec{v}$ is the viscous term which resists the motion of the fluid particles.

Solving above equations (1) and (2) require spatial and temporal discretization together-with pressure-velocity coupling schemes. This can be used to interpolate pressures at the faces of a control volume. Pressure-based solver is used with PISO (Pressure-Implicit with Splitting of Operators) coupling. For spatial discretization, second order pressure, and for momentum second order upwind was used. For gradient discretization, least square cell-based method was used. Implicit formulation is used in discretizing equations. Implicit time marching scheme was employed using second order backward Euler derivative formulation.

The governing equations relevant for the structural mechanics part are as follows:

$$\{\sigma\} = \mathrm{E}\,\{\varepsilon\} \tag{3}$$

where *E* is the stiffness matrix, σ is the stress vector and ε are the strains. The linear stress- strain law is applied to get deformation on the body. Newmark Integration scheme is used to solve non-linear equations and therefore implicit solver is needed to reach towards a solution. Implicit time marching scheme is used together-with Newton-Raphson method for loads and displacement convergence. Newton-Raphson equation is given as follows

$$\mathrm{x_{n+1}} = \mathrm{x_n} - \frac{\mathrm{f(x_n)}}{\mathrm{f'(x_n)}} \tag{4}$$

Equation (4) is used to converge forces, moments and displacements at each timesteps, which works by the principle that the energy added due to the external loads must eventually balance the energy induced by the reaction forces. Governing condition for FSI coupling is the kinematic coupling condition [15] in which no slip condition with the fluid and structure interface was followed. The FSI equations for the kinematic coupling at the interface Γ are given as follows (15):

$$u_\Gamma(t) = d_\Gamma^F(t) \quad (5)$$

$$u'_\Gamma(t) = v_\Gamma(t) \quad (6)$$

$$u''_\Gamma(t) = v_\Gamma(t) \quad (7)$$

Here $d_\Gamma^F(t)$ is the displacement of the fluid mesh at the interface. The dynamic coupling is given by:

$$\sigma^f . n^f + \sigma^s n^s = 0 \quad (8)$$

where σ^f is stress tensor on the fluid side n^i is the normal vector and σ^s is stress tensor on the solid side. The product $\sigma^i . n^i$ is called the traction vector. Due to displacements, dynamic meshing adaptability is needed so that the moving cells on the fluid and solid side could be re-meshed correctly thereby preserving shape quality. Diffusion based smoothing was used with diffusion parameter equal to 2.

2.5 Boundary Conditions and Tumor Growth Modeling

The boundary conditions were used to make the model as realistic as possible. Our model consisted of two inlets and two outlets each of $3mm^2$ diameter. These inlets were defined in the later ventricles whereas outlets were defined in the fourth ventricle. We knew that the inside linings of walls of ventricles have the Choroid Plexus; and in reality, the inside walls behave as a source for CSF. Whereas in this study, inlets were defined at particular points (Fig 4), which is consistent with the previous studies [7,10,12]. This is due to the fact that the behavior of CSF fluid flow is largely a creeping flow [7,10]. The flow is consequently assumed to be in the laminar region throughout [7]. Therefore, in any case, defining the entire inside walls of lateral ventricles as inlet has no ultimate bearing on velocity profile across the CA.

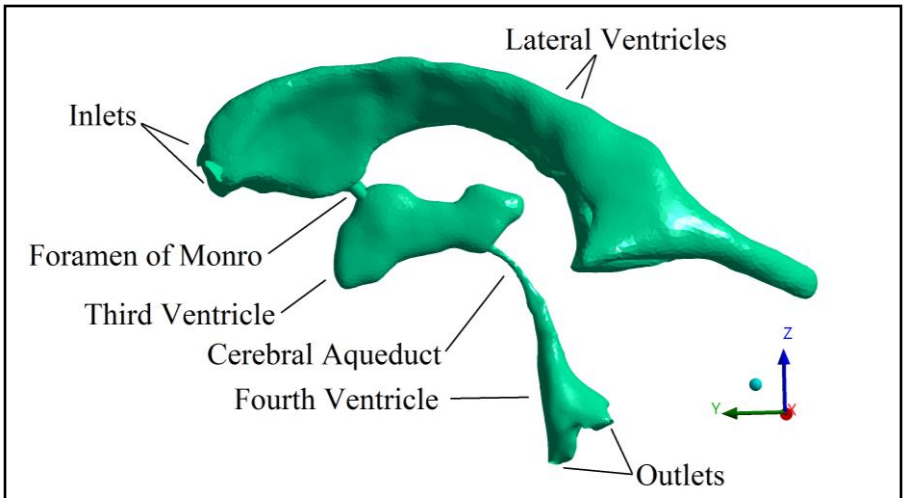

Fig 4. Boundary conditions. All surfaces except the inlets and outlets were part of the FSI interface.

At the fluid side, mass flow inlet boundary condition with bulk production of 500 ml/day (or 6.25×10^{-6} kg/s) was used to mimic the real scenario of CSF flow [16]. While at the outlet, static pressure of 0 Pa was defined [11]. CSF behaves very similar to water in terms of nature [15] with a density of about 1000 kg/m^3 and a constant viscosity of 0.00103 Pa.s. Whereas, the protein content has very limited and negligible effect [15]. CSF was therefore, treated as Newtonian fluid. A Newtonian fluid is usually described by Newton's law of viscosity presented in mathematical form as:

$$\sigma = \mu \frac{du}{dy} \tag{9}$$

where σ is the shear stress, du/dy is the gradient of shear strain and μ is the dynamic viscosity constant.

Equation (9) suggests that if shear stress is directly proportional to rate of shear strain, then fluid will behave as Newtonian fluid. This means that the shear stress along the walls would be maximum and the fluid which is in contact with the medium has zero velocity/strain relative to the wall. This is hence, a no-slip condition. While the shear strain along the wall will be zero.

To add more value to this study, a novel schematic boundary condition was employed i.e. using CSF pulsatility induced during cardiac cycle and its effect on the stenosis of CA. The pulsatile component is ideally a linear combination of sinusoidal harmonics given as [17]:

$$\text{Volumetric flow rate (t)} = \text{Bulk production} + A\sin(wt + \alpha) + B\sin(2wt + \beta) \quad (10)$$

In equation (10), bulk production, as noted above, is approximately equal to 0.3 ml/min ($6.25\text{x}10^{-6}$ kg/sec), A is equal to 0.21 ml/min ($3.5\text{x}10^{-6}$), and B is the part of second harmonic and is taken with an amplitude of 0.05ml/min [17]. Carotid artery, which takes blood away from heart has zero phase difference [17], similar to the CSF flowrate phase in C-2 vertebral column level [17]. However, CSF velocity in the cerebral aqueduct has a phase difference. α and β were assumed to be zero. The pulsatile component was plotted against time and is given by Fig 5.

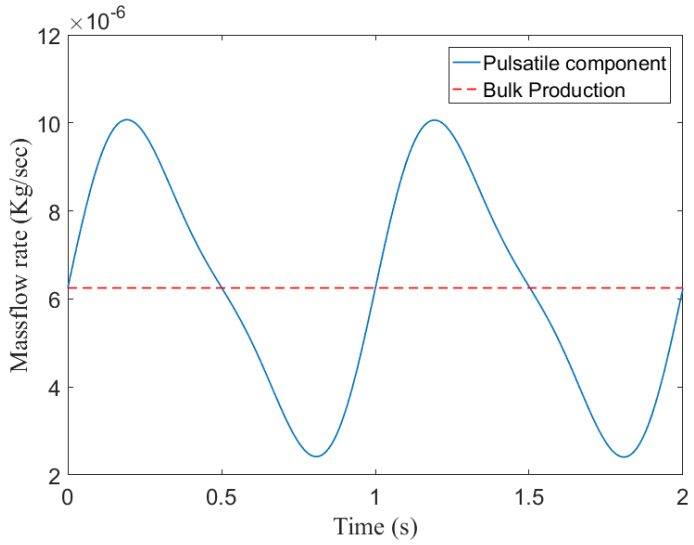

Fig 5. Pulsatile Component of CSF (in mass flowrate) found out using equation (10). Dotted line shows bulk production.

Regarding, the external loading which came from tumor, it is obvious that the initial tumor size needs to be grown in temporal spectrum so that the loading conditions can become dynamic in nature. To predict

the growth of tumor, Gompertz mathematical model is used which is one of the widely used models to extrapolate tumor cells based on the initial tumor volume [18]. The model has the solution of the form as:

$$\text{Volume}(t) = V(0)e^{\frac{\alpha}{\beta}(1-e^{-\beta t})} \tag{11}$$

where, V(0) is the initial tumor volume, α and β are the initial proliferation rate and the exponential decay constants which have values of 0.279 and 0.1470 [19], and t is the time in days.

Figure 6 (a) shows growth of tumor volume over time. From the growth of tumor volume, body forces can be calculated. Body forces can be thought of as forces acting on the entire volume of body such as forces due to the gravity. These forces are basically the weight of the body and can be given by equation (8) as:

$$F = \int \rho g dV \tag{12}$$

where F is the body force, ρ is the density of the tumor mass which is taken to be 1040 kg/m^3 [13], g is acceleration due to gravity (9.81 m/s^2) and dV is the volume differential element. Fig 6 (b) above shows plot of force vs time, found out using equation (12). This force is used in equation (2) as body force.

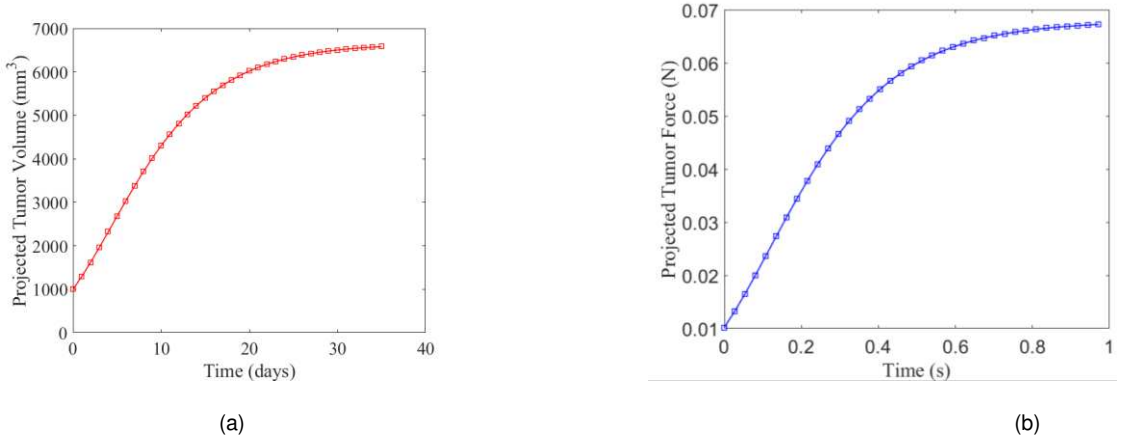

(a) (b)

Fig 6. Tumor growth modeling. (a) shows tumor grown for 35 days using Gompertz model; (b) shows associated force in 0-1 timescale.

2.6 Fluid-Solid Interface

To setup the simulation, solid and fluid domains were set-up separately, where CSF was referred as fluid domain and ventricular walls as the solid domain. Fluid-solid interface boundary was defined by creating a surface Ωs such that it acts as a coupling, where two variables (forces and displacements) were transferred at each timestep. The complete ventricular surface except inlets and outlets were defined as a FSI surface.

LIST OF ABBREVIATIONS

CNS	Central Nervous System
CA	Cerebral Aqueduct
CSF	Cerebrospinal Fluid
CFD	Computational Fluid Dynamics
FSI	Fluid-Structure Interaction
HVS	Human Ventricular System
IBM	Immersed Boundary Method
ICP	Intracranial Cerebral Pressures
MRI	Magnetic Resonance Imaging

DECLARATIONS

Ethics approval and consent to participate

The patient voluntary consented to their data being used for the purpose of this research.

Consent for publication

Not Applicable

Availability of data and materials

The datasets used and/or analysed during the current study are available from the corresponding author on reasonable request.

Competing interests

The authors declare that they have no competing interests

Funding

This project was funded by Higher Education Commission, in the NRPU category. Grant Code: 9984

Authors' contributions

M. Uzair and A. Ahmed worked on the methods and analytical aspect of paper. Z. Mustansar worked on reviewing this manuscript, acquired funding for this research and supervised the entire study. Z. Mustansar and A. Shaukat worked on organization of paper as well. F. Nadeem provided MRI datasets for this research. J. Iqbal Khan contributed to material properties and behavior of the models. S. Talay participated in writing and formatting the manuscript. S. Cukovic and L. Margetts reviewed the manuscript.

Acknowledgements

We are thankful to HEC Pakistan, for providing us funding to execute this research. We are also indebted to the National University of Sciences & Technology (NUST) for providing Computer Labs and logistic support necessary to conduct this study.

Authors' information (optional)

Muhammad Uzair Ul Haq was born in Islamabad, Pakistan. He received the B.E. degree in mechatronics engineering from National University of Sciences and Technology, Islamabad, in 2017. He has obtained his master's degree in Biomedical engineering from National University of Sciences and Technology, Islamabad. His research interest includes computer vision, biomedical imaging, machine learning and robotics.

Ali Ahmed was born in Karachi, Pakistan. He received the B.E. degree in mechatronics engineering from National University of Sciences and Technology, Islamabad, in 2017. He has obtained his master's degree in Biomedical engineering from National University of Sciences and Technology, Islamabad. His research interest includes computational biomechanics, deep learning, robotics and artificial intelligence.

Zartasha Mustansar is currently working as an Assistant Professor at the National University of Science and Technology (NUST) Islamabad in Research Center for Modeling & Simulation (RCMS) since 2013. She received her PhD from the University of Manchester, UK. Zartasha Mustansar pursued her PhD under the prestigeous Micorosft Ressearch Cambridge (MSR), and Dorothy Hodgkin award, in Physical Sciences & Engineering at Manchester. Currently she is contributing to Biomedical engineering/Computational Biomechanics research. She is specially pursuing areas of Finite Elements and Image based modeling. She is also certified in HPC's utility, on Horace and DIESA at Manchester and Scotland respectively. Her research interests include image based modeling, finite element methods, modeling and simulation, computational biomechanics, advanced biomechanical systems and musculo-skeleton modeling.

Arslan Shaukat received the BS and MS degrees in Computer Engineering from National University of Science and Technology (NUST), Islamabad, Pakistan in 2003 and 2005 respectively, and PhD in Computer Science from The University of Manchester, UK in 2010. Currently, he is Assistant Professor in Department of Computer and Software Engineering, CEME, National University of Science and Technology (NUST), Islamabad, Pakistan. He has published various academic papers in refereed journals and conference proceedings. He has been a member of technical program committees of numerous international conferences and is also a reviewer of various IEEE journals and transactions. He jointly chaired the AI and IT convergence session at IEEE ITEC 2019 conference held in Korea. He is a recipient of academic awards including Best Teacher award in 2018 and Best Research Paper award in 2019. His research interests include Machine Learning, Pattern Recognition, Digital Image and Speech Processing.

Competing Interests Statement

Authors declare no conflict of interests.

REFERENCES

[1]. (2021). Cancer Net. Accessed: Feb. 2021. [Online]. Available: https://www.cancer.net/cancer-types/brain-tumor/statistics

[2]. (2021). Hydrocephalus Association. Facts and Stats. Jan. 2021. [Online]. Available https://www.hydroassoc.org/about-us/newsroom/facts-and-stats-2/

[3]. Jacobson, E. E., Fletcher, D. F., Morgan, M. K., & Johnston, I. H. (1996). Fluid dynamics of the cerebral aqueduct. Pediatric neurosurgery, 24(5), 229-236.

[4]. L. Fin and R. Grebe, "Three-dimensional modeling of the cerebrospinal fluid dynamics and brain interactions in the aqueduct of Sylvius," Computer methods in biomechanics and biomedical engineering, vol. 6, pp. 163-170, 2003.

[5]. J. Tu, G. H. Yeoh, and C. Liu, Computational fluid dynamics: a practical approach: Butterworth-Heinemann, 2018.

[6]. A. A. Linninger, C. Tsakiris, D. C. Zhu, M. Xenos, P. Roycewicz, Z. Danziger, et al., "Pulsatile cerebrospinal fluid dynamics in the human brain," IEEE Transactions on Biomedical Engineering, vol. 52, pp. 557-565, 2005.

[7]. Howden, L., Giddings, D., Power, H., Aroussi, A., Vloeberghs, M., Garnett, M., & Walker, D. (2008). Three-dimensional cerebrospinal fluid flow within the human ventricular system. Computer methods in biomechanics and biomedical engineering, 11(2), 123-133.

[8]. Kurtcuoglu, V., Poulikakos, D., Ventikos, Y. (2005). Computational modeling of the mechanical behavior of the cerebrospinal fluid system. J. Biomech. Eng. 127(2), 264–269.

[9]. Jacobson, E. E., Fletcher, D. F., Morgan, M. K., & Johnston, I. H. (1999). Computer modelling of the cerebrospinal fluid flow dynamics of aqueduct stenosis. Medical & biological engineering & computing, 37(1), 59-63.

[10]. Masoumi, N., Bastani, D., Najarian, S., Ganji, F., Farmanzad, F., & Seddighi, A. S. (2010). Mathematical modeling of CSF pulsatile hydrodynamics based on fluid–solid interaction. IEEE transactions on biomedical engineering, 57(6), 1255-1263.

[11]. Gholampour S. FSI simulation of CSF hydrodynamic changes in a large population of non-communicating hydrocephalus patients during treatment process with regard to their clinical symptoms. PloS one. 13(4), 2018.

[12]. Sweetman, B., & Linninger, A. A. (2011). Cerebrospinal fluid flow dynamics in the central nervous system. Annals of biomedical engineering, 39(1), 484-496.

[13]. B. Yang, K.-M. Tse, N. Chen, L.-B. Tan, Q.-Q. Zheng, H.-M. Yang, et al., "Development of a finite element head model for the study of impact head injury," BioMed research international, vol. 2014, 2014.

[14]. Batchelor CK, Batchelor GK. An introduction to fluid dynamics. Cambridge university press; 2000.

[15]. Bodnár T, Galdi GP, Nečasová Š, editors. Fluid-structure interaction and biomedical applications. Springer Basel; 2014.

[16]. J. Tu, G. H. Yeoh, and C. Liu, Computational fluid dynamics: a practical approach: Butterworth-Heinemann, 2018.

[17]. Wagshul, M. E., Chen, J. J., Egnor, M. R., McCormack, E. J., & Roche, P. E. (2006). Amplitude and phase of cerebrospinal fluid pulsations: experimental studies and review of the literature. Journal of neurosurgery, 104(5), 810-819.

[18]. S. Benzekry, C. Lamont, A. Beheshti, A. Tracz, J. M. Ebos, L. Hlatky, et al., "Classical mathematical models for description and prediction of experimental tumor growth," PLoS Comput Biol, vol. 10, p. e1003800, 2014.

[19]. H. Murphy, H. Jaafari, and H. M. Dobrovolny, "Differences in predictions of ODE models of tumor growth: a cautionary example," BMC cancer, vol. 16, pp. 1-10, 2016.

[20]. Abbey, P., Singh, P., Khandelwal, N., & Mukherjee, K. K. (2009). Shunt surgery effects on cerebrospinal fluid flow across the aqueduct of Sylvius in patients with communicating hydrocephalus. Journal of Clinical Neuroscience, 16(4), 514-518.

[21]. Algin, O., Hakyemez, B., & Parlak, M. (2010). The efficiency of PC-MRI in diagnosis of normal pressure hydrocephalus and prediction of shunt response. Academic radiology, 17(2), 181-187.

[22]. Lee, J. H., Lee, H. K., Kim, J. K., Kim, H. J., Park, J. K., & Choi, C. G. (2004). CSF flow quantification of the cerebral aqueduct in normal volunteers using phase contrast cine MR imaging. Korean journal of radiology, 5(2), 81-86.

[23]. Holmlund, "Fluid dynamic principles for analysis of intracranial pressure control: application towards space medicine and hydrocephalus," Umeå Universitet, 2019.

[24]. Masoumi, N., Bastani, D., Najarian, S., Ganji, F., Farmanzad, F., & Seddighi, A. S. (2010). Mathematical modeling of CSF pulsatile hydrodynamics based on fluid–solid interaction. IEEE transactions on biomedical engineering, 57(6), 1255-1263.

[25]. Takizawa, K., Matsumae, M., Sunohara, S., Yatsushiro, S., & Kuroda, K. (2017). Characterization of cardiac-and respiratory-driven cerebrospinal fluid motion based on asynchronous phase-contrast magnetic resonance imaging in volunteers. Fluids and Barriers of the CNS, 14(1), 25.

[26]. Aktas, G., Kollmeier, J. M., Joseph, A. A., Merboldt, K. D., Ludwig, H. C., Gärtner, J., ... & Dreha-Kulaczewski, S. (2019). Spinal CSF flow in response to forced thoracic and abdominal respiration. Fluids and Barriers of the CNS, 16(1), 10.